



## Surface rock effects on soil moisture retrieval from L-band passive microwave observations



N. Ye<sup>a</sup>, J.P. Walker<sup>a,\*</sup>, C. Rüdiger<sup>a</sup>, D. Ryu<sup>b</sup>, R.J. Gurney<sup>c</sup>

<sup>a</sup> Department of Civil Engineering, Monash University, Australia

<sup>b</sup> Department of Infrastructure Engineering, University of Melbourne, Australia

<sup>c</sup> Environmental Systems Science Centre & National Centre for Earth Observation, University of Reading, United Kingdom

### ARTICLE INFO

**Keywords:**  
 Passive microwave  
 Soil moisture  
 Remote sensing  
 Rock fraction  
 SMOS  
 SMAP

### ABSTRACT

The L-band (1.41 GHz) passive microwave remote sensing technique is the approach used by the first satellites dedicated to soil moisture measurement, the European Space Agency's (ESA) Soil Moisture and Ocean Salinity (SMOS), and the Soil Moisture Active Passive (SMAP) mission developed by the National Aeronautics and Space Administration (NASA). These satellites aim to provide global soil moisture maps for the top ~5 cm layer of soil with an accuracy better than  $0.04 \text{ m}^3/\text{m}^3$ . However, with a passive microwave observing resolution of ~40 km, non-soil targets such as surface rock may possibly confound the brightness temperature observations and degrade the accuracy of retrievals for many SMOS and SMAP pixels across the world. Since the microwave contribution of rock is not well accounted for in current soil moisture retrieval algorithms, simply ignoring its existence may be detrimental to the performance of resultant soil moisture products. Using a combination of model simulations and airborne field campaign data from central Australia, this study has determined that a rock cover fraction threshold of up to 0.4 can be tolerated before the  $0.04 \text{ m}^3/\text{m}^3$  soil moisture target accuracy is potentially exceeded under extreme dry or wet conditions. However, this threshold reduces to 0.2 when assessed in terms of a brightness temperature impact  $> 4 \text{ K}$ . These rock fraction thresholds have subsequently been applied to the Ecoclimap rock cover map, identifying the SMOS and SMAP pixels globally that are likely to be adversely affected if rock is unaccounted for. The results show that approximately ~3.3% of all SMOS and SMAP pixels may have brightness temperature impacts exceeding 4 K from surface rock, with Asia being the most affected, having ~6.0% affected pixels. These values reduce to ~1.5% of SMOS and SMAP pixels globally, and ~3.1% for Asia, when assessed in terms of soil moisture errors expected to possibly exceed  $0.04 \text{ m}^3/\text{m}^3$  when not accounting for surface rock.

### 1. Introduction

Soil moisture is a key variable in global water, energy, and carbon cycling, which is fundamental to hydrology, meteorology, and agriculture (Sellers et al., 1997). Due to its high variability in time and space, it is difficult to measure or predict the spatial and temporal distribution of soil moisture at regional and global scales (Crow et al., 2012; Ryu and Famiglietti, 2006). However, the first satellite dedicated to measuring global soil moisture was launched on November 2nd, 2009. This Soil Moisture and Ocean Salinity (SMOS) mission, led by the European Space Agency (ESA) in collaboration with the Centre National d'Etudes Spatiales (CNES) in France and the Centro para el Desarrollo Tecnológico Industrial (CDTI) in Spain, measures soil water content in the top ~5 cm soil every 2 to 3 days with a target accuracy of better than  $0.04 \text{ m}^3/\text{m}^3$ , using a 2-D interferometric radiometer operating at

L-band (1.413 GHz; Kerr et al., 2010). Likewise the National Aeronautics and Space Administration (NASA) developed the Soil Moisture Active Passive (SMAP) mission to measure soil moisture using a combination of L-band (1.41 GHz) radiometer and L-band (1.26 GHz) radar to increase the resolution of soil moisture products from 40 km to 10 km (Entekhabi et al., 2010). Since the approach was to first downscale the brightness temperature measurements according to the spatial patterns in the radar data, with the soil moisture then retrieved using the standard passive microwave algorithms, any errors in the radiometer data at the native resolution would be carried through to the higher resolution products. Even though the radar unfortunately malfunctioned shortly after launch, this same issue applies to the alternative downscaling approaches currently being proposed.

The passive microwave remote sensing technique has been adopted for soil moisture measurement as it is unaffected by cloud, has a direct

\* Corresponding author.

E-mail address: [jeff.walker@monash.edu](mailto:jeff.walker@monash.edu) (J.P. Walker).

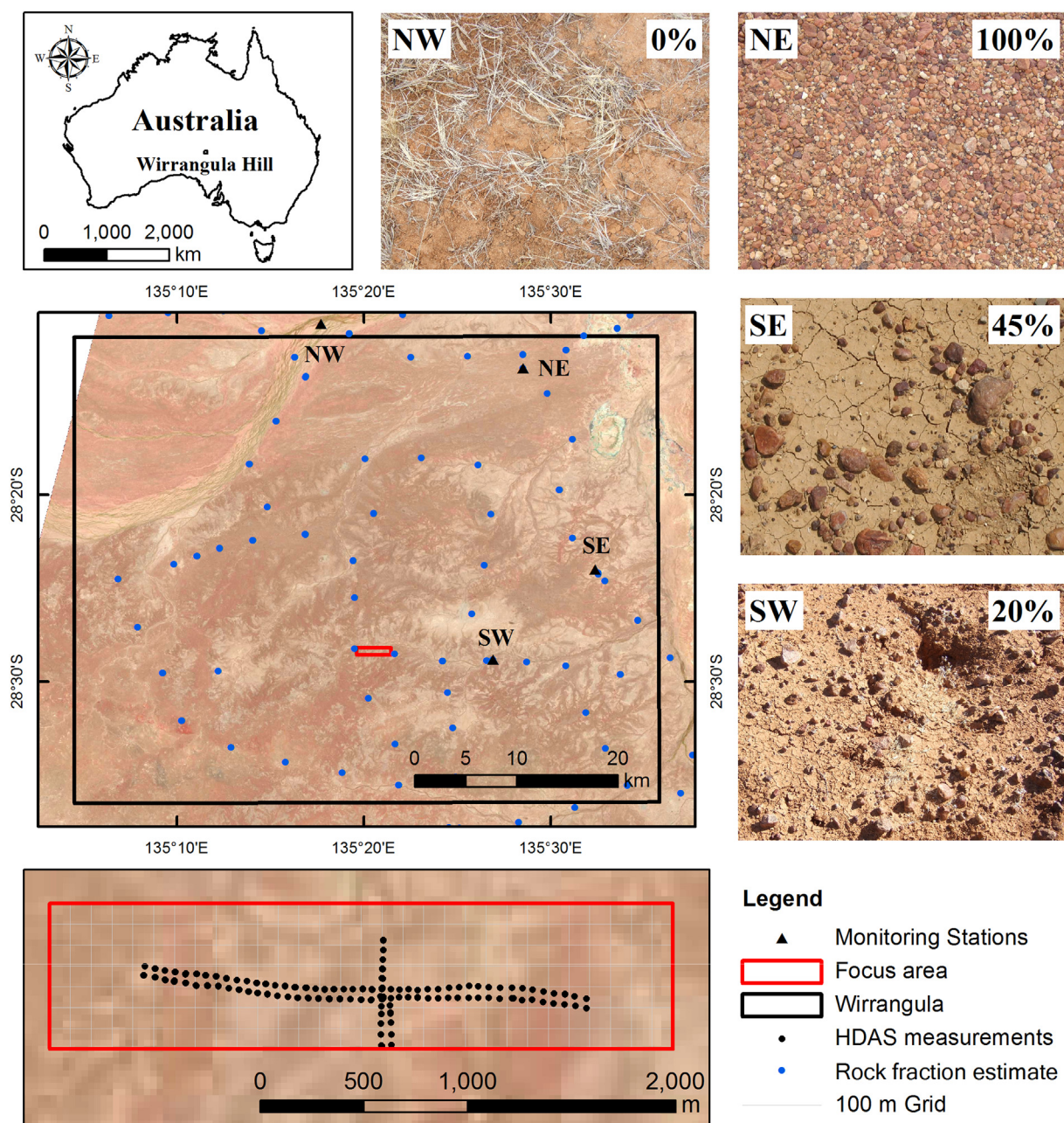


**Fig. 1.** Location of the Wirrangula Hill study area within Australia (top left), the focus area (red box, middle left), temporal monitoring stations (black triangles, middle left), and the HDAS measurements (black dots, bottom left). Also shown are ground level photographs of the land surface at the monitoring stations as labelled in the top left corner of each picture. (For interpretation of the references to colour in this figure legend, the reader is referred to the web version of this article.)

relationship with soil moisture through the soil dielectric constant, and has a reduced sensitivity to land surface roughness and vegetation canopy, compared with optical, infrared, and active microwave techniques (Jackson and Schmugge, 1989; Njoku et al., 2002). However, the spatial resolution of L-band space-borne radiometer measurements is restricted by the size of antenna, meaning that a resolution on the order of ~40 km is achieved based on the current level of antenna technology. For the SMOS mission, 69 elementary radiometers are distributed along three Y-shaped arms of 4.5 m in length, to produce an elliptical shaped footprint of ~43 km in size using synthetic aperture techniques. In contrast, the SMAP mission uses a rotating mesh antenna of 6 m (20 ft) in diameter to directly observe a single brightness temperature of ~40 km spatial resolution.

The volumetric soil moisture of each SMOS and SMAP radiometer pixel is subsequently retrieved from the brightness temperature

observations through the use of radiometric transfer models. Although the SMOS soil moisture retrieval algorithm is capable of three different surface types (bare soil, vegetated soil, and forest) within the SMOS footprint (Kerr et al., 2010; Kerr et al., 2012), the accuracy of the SMOS and SMAP soil moisture retrieval will suffer from land surface heterogeneity at such a coarse scale. In addition, the impacts of surface rock, standing water, and urban areas within the sensor's field of view have not been well studied and accounted for in the current soil moisture retrieval models, causing an uncertainty in the soil moisture retrieval accuracy (Delwart et al., 2008). While a few model simulation studies have been performed to explore the rock cover fraction threshold for the SMOS target soil moisture accuracy of  $0.04 \text{ m}^3/\text{m}^3$  (Kerr et al., 2010; Loew, 2008), there has been no rigorous assessment of the expected rock impact globally. The rock fraction thresholds of 0.11 and 0.15–0.20 were obtained from Kerr et al. (2010) and Loew (2008)

respectively, assuming that rock behaves as very dry bare soil with a fixed dielectric constant and roughness, but these results have not been confirmed through field data.

According to dielectric constant measurements on a range of rock types at a frequency of 400 MHz and 35 GHz, the real part of the dielectric constant of rock ranges from 2.4 to 9.6 (Ulaby et al., 1986). A value of  $5.7 - j \times 0.074$  has been suggested in the SMOS Algorithm Theoretical Basis Document (ATBD) as an appropriate value for the dielectric constant of rock (Kerr et al., 2010). To date only a few experiments (e.g. Cano et al., 2010; Jackson et al., 1992; Monerris et al., 2008) have been conducted to explore the impact of surface rock on L-band brightness temperature observations. These have found that i) rock has a very low porosity meaning that it does not absorb any appreciable amount of water; ii) the low dielectric constant of rock reduces the effective dielectric constant of the wet soil surface mixed with rocks; iii) the presence of rock results in an increase of soil surface roughness; and iv) no improvement of soil moisture retrieval accuracy was found for brightness temperature modelling if rocks were assumed as a smooth surface with a fixed dielectric constant. The joint impact of these four aspects makes microwave emission from the rock covered land surface complex.

The objective of this study was to further investigate the effect of rock on brightness temperature observation and soil moisture retrieval accuracy using both synthetic and observational data from a field experiment. These results were then used to demonstrate the expected impact of rock on L-band brightness temperature observation and soil moisture retrieval accuracy globally, by identifying SMOS and SMAP pixels with rock-induced brightness temperature contribution in excess of the 4 K, which is equal to the SMOS brightness temperature error budget, and/or soil moisture error in excess of the  $0.04 \text{ m}^3/\text{m}^3$  target soil moisture accuracy of SMOS and SMAP missions (Entekhabi et al., 2010; Kerr et al., 2010). Consequently, these maps can be used to mask or flag adversely affected pixels in the absence of accounting for rock in the soil moisture retrieval process.

## 2. Data sets and study areas

The airborne passive microwave observations, ground sampling data, and monitoring stations measurements collected during the SMOS Arid Zone Experiment in Australia 2009 (Rüdiger et al., 2014) were used in this study to validate the rock fraction effect determined from model simulation. The field experiment was conducted in August 2009 over three  $50 \text{ km} \times 50 \text{ km}$  study areas in central Australia, aiming to identify vicarious calibration sites for the on-orbit calibration of SMOS using airborne passive microwave data and in-situ measurements. The study area known as Wirrangula Hill is characterized by very sparse vegetation and up to 90% rock pavement cover known as “gibber”, ranging in diameter from 2 cm to 20 cm, as shown in Fig. 1. Passive microwave observations were collected over the study area using the Polarimetric L-band Multi-beam Radiometer (PLMR) mounted on a scientific aircraft. The PLMR is a dual-polarized (horizontally and vertically) radiometer with six beams having viewing angles of  $\pm 7^\circ$ ,  $\pm 21.5^\circ$  and  $\pm 38.5^\circ$ , measuring microwave radiation at L-band (1.413 GHz) in a bandwidth of 24 MHz. In push-broom configuration, all six beams of the PLMR are distributed in an across-track direction to either side of the aircraft. Each beam has an along-track beamwidth of  $17^\circ$  and across-track beamwidth of  $14^\circ$ , yielding a swath width of approximately two times the aircraft altitude above the ground, and a resolution of approximately one-third of the altitude. The calibration of the PLMR was performed before and after each flight, using cold (the sky) and warm (a temperature-recorded blackbody box) targets. The accuracy of calibrated PLMR observations was found to be 0.7 K for horizontal polarization and 2 K for vertical polarization in the range (150 to 300 K) of brightness temperature observations collected over the land surface during the NAFE'05 campaign (Panciera et al., 2008). Due to their slightly higher side lobe gain, outer beams of vertical

polarization were easier to be affected by noise in the airport during ground calibration, which results in lower accuracy than horizontal polarization. On the single sampling day over the Wirrangula Hill study area, 12 August 2009, the airborne passive microwave observations were collected at 1000 m resolution over the entire study area and at  $\sim 100$  m resolution over a  $700 \text{ m} \times 3000 \text{ m}$  focus area. In addition, visual estimates and photographs of ground rock fraction collected during a field experiment over the Wirrangula Hill study area (Walker et al., 2003) were used to obtain the spatial distribution of rock cover fraction.

Coincident with the flight, top  $\sim 5$  cm soil moisture was sampled on the ground at a spacing of  $\sim 50$  m across the focus area using the Hydraprobe Data Acquisition System (HDAS; Panciera et al., 2006). The HDAS was developed to make point measurements of water content in the top 5 cm soil using the frequency-domain reflectometry (FDR) technique. The soil moisture was measured and stored together with the latitude and longitude of the sampling spot automatically using a handheld computer that forms part of the HDAS system. Ancillary data of the vegetation type, vegetation height, and rock cover fraction were also recorded in the HDAS. A volumetric soil moisture accuracy of  $0.035 \text{ m}^3/\text{m}^3$  was determined from an independent calibration check of the universal calibration equation determined by Merlin et al. (2007) using the thermo-gravimetric technique.

The field measurements of soil moisture were used as the reference for comparing brightness temperature derived soil moisture, in order to validate the rock fraction impact under very dry bare soil condition. In addition, four monitoring stations were installed throughout the Wirrangula Hill area for the duration of the flight. These included i) Theta probes installed vertically at the surface (top 6 cm) and horizontally at 25 cm depth to give temporal variation of soil moisture, ii) thermocouples for measuring soil temperature at depths of 2.5 cm, 5 cm, 15 cm, 25 cm, and 40 cm for estimating effective soil temperature, iii) leaf wetness sensor for indicating the presence of dew, iv) a thermal infrared radiometer for estimating skin temperature, and v) a pluviometer for measuring rainfall. Surface roughness measurements were made for a continuous 2 m long soil profile in north-south and east-west directions at each monitoring station by measuring surface height variations using a pin profiler, together with a ground level photograph.

Given the stable land surface of the Wirrangula Hill, the distribution of rock cover fraction was assumed to be temporally consistent. During the field experiment in 2003, rock cover fraction was visually estimated at over 160 locations across the study area (blue dots in Fig. 1). Additionally, ground photos were taken for each location to later confirm the estimates of rock cover fraction.

## 3. Soil moisture retrieval model

The volumetric water content in the top 5 cm layer of soil can be retrieved from L-band passive microwave observations using a radiobrightness transfer model such as the L-band Microwave Emission of the Biosphere (L-MEB; Wigneron et al., 2007), Community Microwave Emission Model (CME; de Rosnay et al., 2009), or the Land Parameter Retrieval Model (LPRM; Owe et al., 2001). These models were developed based on the ‘ $\tau$ - $\omega$  model’ (Mo et al., 1982) in which  $\tau$  and  $\omega$  are the optical depth and the single scattering albedo of vegetation canopy respectively. Accordingly, the brightness temperature ( $TB$ ) of the vegetation-soil layer is defined as the sum of i) the upward emission from the vegetation layer scattered by the atmosphere; ii) the downward emission from the vegetation layer reflected by the soil surface, attenuated by the vegetation layer itself, and then scattered by the atmosphere; and iii) the upward emission from soil layer attenuated by the vegetation layer:

$$TB_p = (1 - \omega_p) \cdot (1 - \gamma_p) \cdot T_v + (1 - \omega_p) \cdot (1 - \gamma_p) \cdot \Gamma_p \cdot \gamma_p \cdot T_v + (1 - \Gamma_p) \cdot \gamma_p \cdot T_s, \quad (1)$$

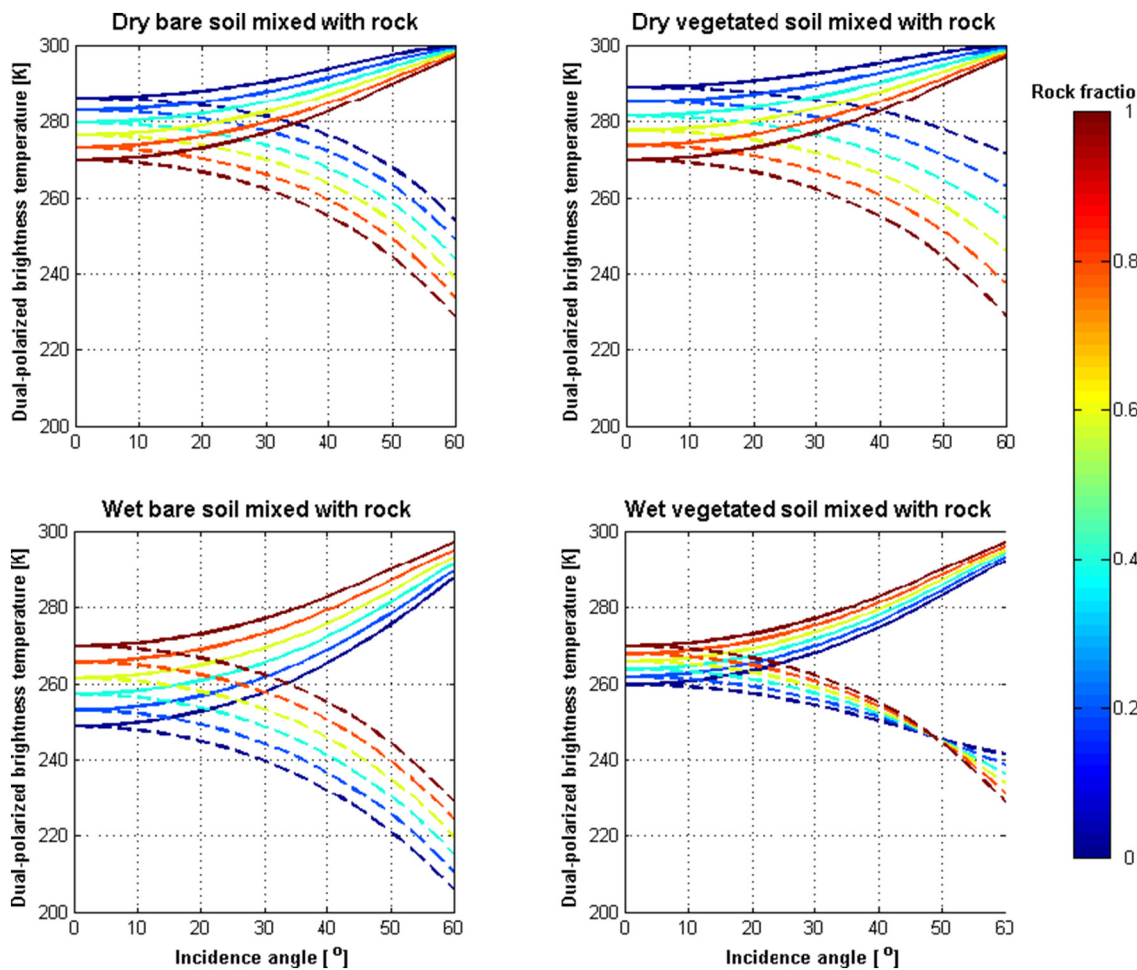


**Fig. 2.** Rock fraction impact on the brightness temperature (solid lines for vertical polarization and dashed lines for horizontal polarization) according to incidence angle for four synthetic scenarios, with rock fraction from 0 to 1 with 0.2 steps.

where  $T_v$  and  $T_s$  are the effective temperatures of vegetation and soil layers, and  $\gamma$  and  $\Gamma$  are the transmissivity of the vegetation layer and reflectivity of soil surface respectively. The subscript  $p$  indicates the polarization, either horizontal (H) or vertical (V). The transmissivity  $\gamma$  of the vegetation layer is a function of the vegetation optical depth at nadir ( $\tau_{NAD}$ ), incidence angle ( $\theta$ ), and the vegetation structure coefficient ( $tt$ ), given as (Wigneron et al., 2007):

$$\gamma_p = \exp[-\tau_{NAD} \cdot (tt_p \cdot \sin^2(\theta) + \cos^2(\theta)) \cdot \cos^{-1}(\theta)]. \quad (2)$$

The optical depth  $\tau_{NAD}$  has been shown to be linearly dependent on the Vegetation Water Content (VWC) and a coefficient  $b$  (Jackson and Schmugge, 1991; Van de Griend and Wigneron, 2004), defined as:

$$\tau_{NAD} = b \cdot VWC. \quad (3)$$

Additionally, the Fresnel equations are used to calculate the reflectivity of the specular surface ( $\Gamma^*$ ) using the incidence angle from nadir and the relative dielectric constant of the material. The dielectric constant of soil is a complex value, whose real part varies with soil moisture ( $SM$ ) from  $\sim 4$  for very dry soil to  $\sim 40$  for very wet soil. Using one of the dielectric mixing models (e.g. Dobson et al., 1985; Mironov et al., 2004; Wang and Schmugge, 1980), the dielectric constant of soil at L-band can be estimated from the soil moisture, soil texture, and soil bulk density. In this study, the Dobson et al. (1985) dielectric mixing model was used in the  $\tau\omega$  model. The roughness of the soil surface is taken into account through the parameters  $HR$  and  $NR$  (Wang and Schmugge, 1980; Wigneron et al., 2001) by:

$$\Gamma_p = \Gamma_p^* \cdot \exp[-HR \cdot \cos^{NR_p}(\theta)]. \quad (4)$$

Soil moisture can thus be retrieved from L-band passive microwave observations using an iterative method for minimizing the difference between observed and model simulated brightness temperatures. Moreover, soil moisture can be retrieved together with other parameters such as vegetation optical depth and surface roughness when using dual polarized and/or multi-incidence angle brightness temperature.

#### 4. Methodology

In this paper, rock was assumed to behave as soil but with the fixed dielectric constant of  $5.7-j \times 0.074$  (Jackson et al., 1992; Kerr et al., 2010; Ulaby et al., 1986), and thus the brightness temperature of rock was estimated as soil using the L-MEB. The overall brightness temperature of a rock mixed pixel (bulk brightness temperature  $TB_{Bp}$ ) is defined as the sum of rock component ( $TB_{Rp}$ ) and soil component ( $TB_{Sp}$ ) weighted by the rock cover fraction ( $f_R$ ) such that

$$TB_{Bp} = f_R \cdot TB_{Rp} + (1 - f_R) \cdot TB_{Sp}. \quad (5)$$

Similarly, the mean soil moisture of the entire pixel is defined as the bulk soil moisture.

$$SM_B = (1 - f_R) \cdot SM_S, \quad (6)$$

where  $SM_S$  is the water content of the soil component alone. Subsequently, the rock induced soil moisture retrieval error is defined as the difference between retrieved soil moisture with and without accounting for the presence of rock.

The effect of surface rock on brightness temperature and soil moisture retrieval accuracy was first simulated under different soil moisture and vegetation scenarios. Second, the synthetic rock effects were validated using airborne brightness temperature observations and ground soil moisture measurement over the Wirrangula Hill study area. Finally, a threshold of rock cover fraction was obtained for the SMOS and SMAP soil moisture target accuracy of  $0.04 \text{ m}^3/\text{m}^3$ , and used to estimate the rock induced soil moisture errors for SMOS pixels globally.

## 5. Results

### 5.1. Synthetic study of rock fraction impact on soil moisture retrieval accuracy

A land surface representation consisting of soil and rock components with a rock cover fraction of  $f_R$  was used to simulate the soil moisture retrieval error induced solely by rock. The dual polarized brightness temperature values of the land surface representation were simulated for incidence angles from  $0^\circ$  to  $60^\circ$  for four scenarios including bare and vegetated soil having low and high moisture content mixed with rock (Fig. 2). The parameters used in the L-MEB model are summarized in Table 1, set to typical values in literature (e.g. Kerr et al., 2010; Wigneron et al., 2007). The ancillary data required in the L-MEB are listed in Table 2. Although the parameters values used result in different simulated brightness temperatures, the general trend of brightness temperature against rock cover fraction changes only slightly. The roughness parameters and optical depth of rock were set equal to those of soil for the purpose of simulating the extreme case of rock evenly mixed with vegetated soil. In the next section the actual values for the study area were calibrated.

As expected, the bulk brightness temperature varies from the brightness temperature of the soil component towards that of the rock component with increasing rock cover fraction. For a given rock cover fraction, rock effect on brightness temperature is dependent mainly on the brightness temperature difference between soil and rock components. Given the fixed dielectric constant of  $5.7-j \times 0.074$ , rock behaves like soil with equivalent water content of  $\sim 0.1 \text{ m}^3/\text{m}^3$ . When mixed with very dry soil, the effect of rock is to decrease the overall brightness temperature. In contrast, rock increases the overall brightness temperature when mixed with very wet soil. In the worst-case scenarios of Fig. 2, rock could have a considerable impact on the bulk brightness temperature, with increase in rock fraction by as little as 0.1 introducing brightness temperature differences of up to 2 K.

The rock induced brightness temperature difference is roughly constant over the examined range of incidence angles. However, when vegetated wet soil is mixed with bare rock, the minimum impact of rock is for horizontally polarized brightness temperature at high incidence angles. In most cases, the impact of rock fraction on brightness temperature depends primarily on soil moisture, and secondarily on incidence angle. During the estimation of rock impacts on soil moisture retrieval accuracy later in this paper, the dependence of rock impact only on soil moisture is studied in more detail.

Given the  $40^\circ$  incidence angle of the SMAP radiometer and the  $42.5^\circ$  SMOS L1C product, dual-polarized brightness temperature of the land surface representation at  $40^\circ$  was simulated across a wide range of

**Table 2**

Land surface parameters used in the soil moisture retrieval algorithm for the Wirrangula Hill study area.

Sand content [%]	41.8
Clay content [%]	9.0
Bulk density [ $\text{g}/\text{cm}^3$ ]	0.92
Surface soil temperature [K]	289
Deep soil temperature [K]	291
Vegetation water content [ $\text{kg}/\text{m}^2$ ]	0
Soil moisture [ $\text{m}^3/\text{m}^3$ ]	0.04

water content. To reduce effect of heterogeneity of vegetation, bulk optical depth  $(1 - f_R) \cdot \tau$  was used in the L-MEB, and only soil moisture of the land surface representation was retrieved. The left and middle panels of Fig. 3 illustrate the curves of retrieved soil moisture against the bulk soil moisture as “truth”, for rock cover fraction ranging from 0 to 0.9 with 0.15 steps. It is clear that the soil moisture retrieval model overestimates the bulk soil moisture for dry soil and underestimates for wet soil, when not accounting for the presence of rock. According to Eq. (6), the range of bulk soil moisture is limited by the range of water content possible for the soil component. Under medium-range bulk soil moisture ( $\sim 0.2 \text{ m}^3/\text{m}^3$ ) conditions, rock presence typically induces the lowest soil moisture retrieval errors for most rock cover fractions. In the context of the SMOS and the SMAP soil moisture retrieval target accuracy of  $0.04 \text{ m}^3/\text{m}^3$ , it can be seen that soil moisture retrieval could have an error exceeding the error budgets of SMOS and SMAP under extremely dry and wet conditions, if the presence of rock is not considered in the soil moisture retrieval.

The right panel of Fig. 3 shows the relationship between rock fraction and the maximum absolute soil moisture error for bare and vegetated soil under dry (bulk soil moisture lower than 0.2) and wet (bulk soil moisture higher than 0.2) soil conditions. For the SMOS and SMAP target accuracy of  $0.04 \text{ m}^3/\text{m}^3$ , the rock cover fraction threshold ( $f_{RT}$ ) was derived for each of four simulated scenarios. This threshold varied from 0.09 to 0.43. However, the rock induced soil moisture error for vegetated soil is higher than the  $0.04 \text{ m}^3/\text{m}^3$  target for most of the rock fraction range.

To identify SMOS and SMAP pixels potentially affected by rock induced error in excess of the SMOS and SMAP target accuracy of  $0.04 \text{ m}^3/\text{m}^3$ , a conservative rock fraction threshold of 0.4 was determined.

### 5.2. Validation of rock fraction impact using field experiment data

The effect of rock cover fraction on soil moisture retrieval accuracy was further validated under bare dry soil condition using airborne brightness temperature and ground data collected over the Wirrangula Hill study area. Because of the high variation in rock cover fraction at pixel scale (100 m) across the study area, the first step was to estimate the rock fraction variation across the study area. From the field photographs over the rock soil surface, it was found that the colour of rock was darker than that of soil. Assuming that the darkness of rock and soil is consistent within the study area, the rock fraction was estimated from visible imagery over the entire study area using a relationship between rock fraction and gray-scale intensity. In this study, a Landsat-8 RGB

**Table 1**

The soil moisture (SM), roughness parameters ( $HR$ ,  $NR_h$ , and  $NR_v$ ), soil temperature ( $T_S$ ), vegetation optical depth ( $\tau$ ), vegetation albedo ( $\omega_h$  and  $\omega_v$ ), and vegetation structure parameters ( $tt_h$  and  $tt_v$ ) used for the four synthetic scenarios.

	SM [ $\text{m}^3/\text{m}^3$ ]	HR [-]	NR <sub>h</sub> [-]	NR <sub>v</sub> [-]	T <sub>S</sub> [K]	$\tau$ [-]	$\omega_h$ [-]	$\omega_v$ [-]	tt <sub>h</sub> [-]	tt <sub>v</sub> [-]
Bare dry soil	0.02	0.1	0	0	300	–	–	–	–	–
Bare wet soil	0.2	0.1	0	0	300	–	–	–	–	–
Vegetated dry soil	0.02	0.1	0	0	300	0.12	0.05	0.05	1	1
Vegetated wet soil	0.2	0.1	0	0	300	0.12	0.05	0.05	1	1
Rock	–	0.1	0	0	300	–	–	–	–	–

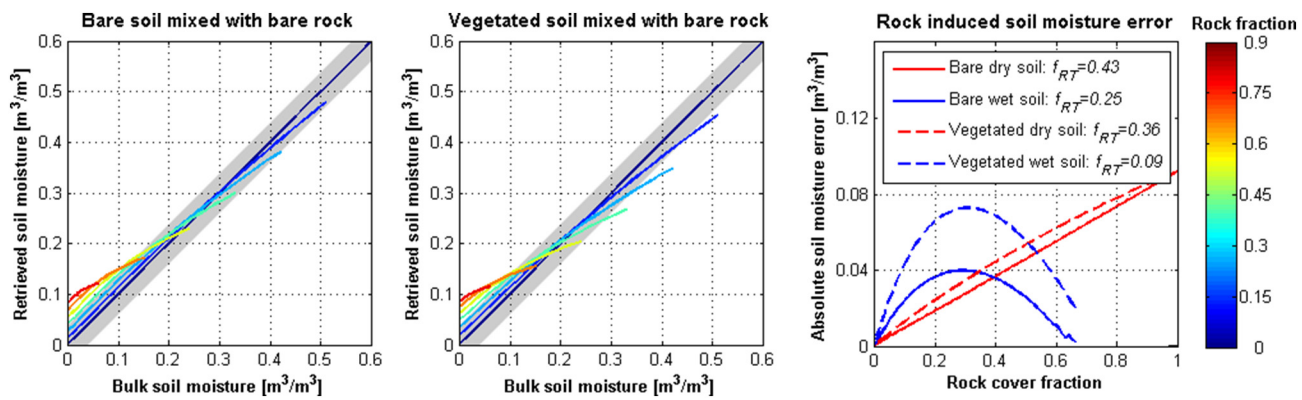


**Fig. 3.** Rock fraction impact on the soil moisture retrieval accuracy for bare (left panel) and vegetated (middle panel) soil scenarios. The curves show bulk soil moisture against retrieved soil moisture for rock cover fraction ranging from 0 to 0.90 with 0.15 steps. The gray shaded areas show the soil moisture accuracy within  $0.04 \text{ m}^3/\text{m}^3$ . The right panel shows the relationship between rock fraction and absolute soil moisture error for bare and vegetated soil under dry (bulk soil moisture  $< 0.2 \text{ m}^3/\text{m}^3$ ) and wet (bulk soil moisture  $> 0.2 \text{ m}^3/\text{m}^3$ ) conditions, with the rock fraction threshold ( $f_{RT}$ ) obtained for the SMOS and SMAP target accuracy of  $0.04 \text{ m}^3/\text{m}^3$ .

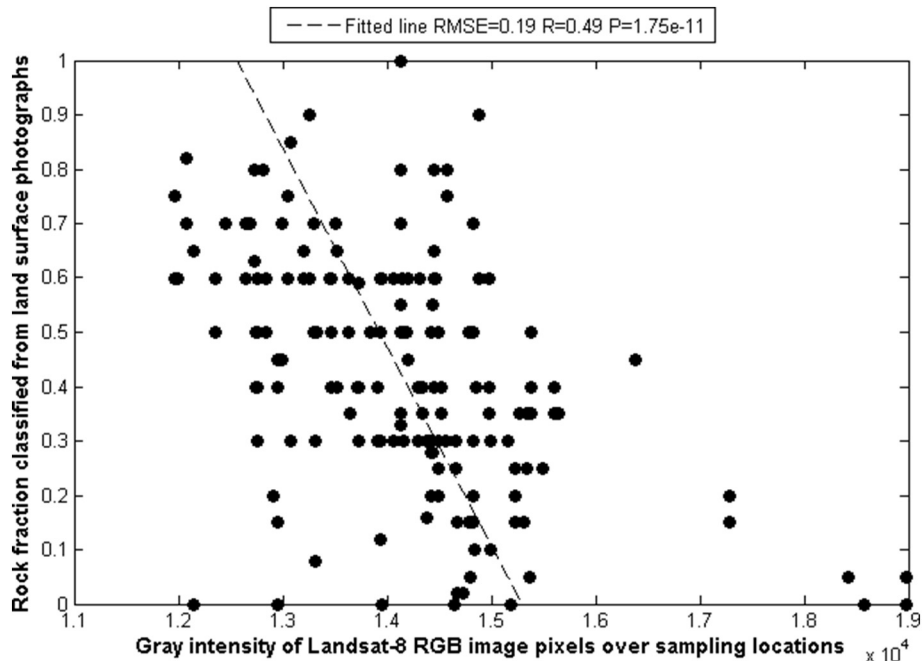


**Fig. 4.** The relationship between rock cover fraction visual estimates and gray scale intensity (16-bit) of corresponding pixels in the Landsat-8 RGB image at the same locations. Root-Mean-Square Error (RMSE), correlation coefficient (R), and statistics P value (P) have been calculated.

**Table 3**

Calibrated roughness parameters for soil and rock components over the Wirrangula Hill study area.

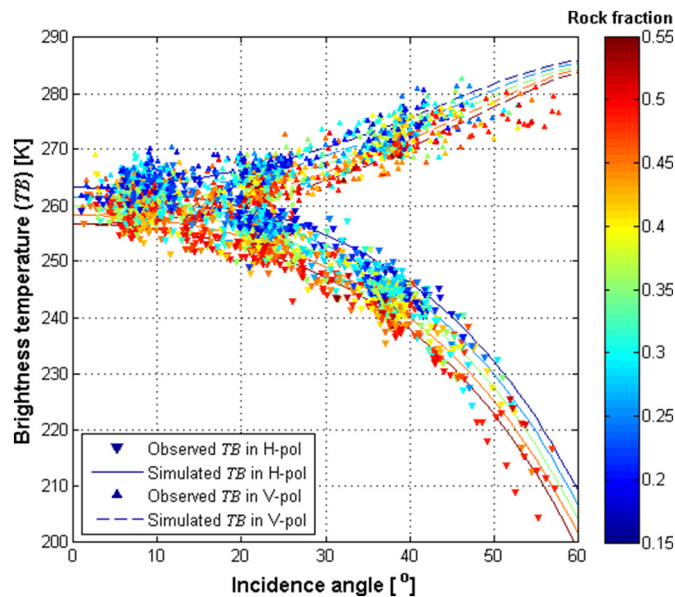
Soil roughness $HR$ [-]	0.04
Soil roughness exponent $NR_H$ [-]	1
Soil roughness exponent $NR_V$ [-]	1
Rock roughness $HR$ [-]	0.24
Rock roughness exponent $NR_H$ [-]	1
Rock roughness exponent $NR_V$ [-]	1

image over Wirrangula Hill collected on 5th Dec. 2013 was used for the gray-scale intensity. Fig. 4 shows the visual ground estimates of rock cover fractions against gray-scale intensities of the corresponding pixels in the geo-referenced Landsat-8 RGB image. A linear model was fitted to the rock fractions versus gray intensities with a rock fraction RMSE of 0.19, correlation coefficient R of 0.49, and P value of  $1.75 \times 10^{-11}$ . This relationship was then applied to the Google Earth image to estimate high resolution rock fraction throughout the entire Wirrangula

Hill study area.

The focus area was divided into a  $7 \times 30$  grid with a resolution of  $100 \text{ m} \times 100 \text{ m}$ , which is close to the scale of the high resolution brightness temperature observations. Each pixel was assumed to be homogeneous and its rock fraction estimated by simply averaging the high resolution rock fraction estimates within it. Subsequently, the multi-angular brightness temperature observations at the high resolution were compared with rock fractions of corresponding  $100 \text{ m}$  pixels. Since the focus area was repeatedly sampled four times with different viewing angles, brightness temperature observations were collected at a range of incidence angle from  $0$  to  $60^\circ$ .

Assuming rock and soil components of all  $100 \text{ m}$  pixels are similar, roughness parameters of soil and rock components were calibrated and listed in Table 3. The brightness temperatures were simulated for incidence angles from  $0^\circ$  to  $60^\circ$  and rock cover fractions of focus area from 0.15 to 0.55 in 0.1 steps using calibrated parameters. Fig. 5 illustrates the angular relationship of the observed and simulated brightness temperature data in dual-polarization, coloured by rock



**Fig. 5.** The angular relationship of observed (symbol) and simulated (line) brightness temperature for various rock fractions (shown by colour).

cover fraction. It is clear that there is a good agreement between the observed and simulated brightness temperature data, and that both observed and simulated brightness temperatures decrease with increasing rock fraction. This result i) showed the roughness of the rock component is much higher than that of the soil; ii) confirmed the rock cover fraction estimates; and iii) demonstrated the impact of rock fraction on brightness temperature.

Compared with the soil component, in Wirrangula Hill the rock had a darker colour, larger particle size and higher dielectric constant. While the first two factors result in an increase in brightness temperature via higher physical temperature and surface roughness, the last factor leads to a decrease. According to Fig. 5, rock fraction had a negative combined impact on brightness temperature, meaning that the dominating factor of rock impact was the higher bulk dielectric constant under very dry bare soil conditions.

To confirm the rock fraction impact on brightness temperature, the brightness temperature data were averaged across all incidence angles in the range of 0° to 60° for each level of rock fraction, as the rock induced brightness temperature difference was found in Fig. 5 to be less sensitive to incidence angle. A second-order polynomial function was fitted to the relationship of brightness temperature observations against their incidence angle for each pixel, in order to minimize the effect of brightness temperature noise on the angular relationship. Subsequently the fitted brightness temperature at the SMAP nominal incidence angle of 40°, as an example, was compared with the corresponding rock fraction in Fig. 6. According to the fitted functions of observed and simulated data, each 0.1 increase of rock fraction caused a decrease of ~2 K and ~1 K in horizontally and vertically polarized brightness temperatures, respectively. This relationship was found to be similar across the 0° to 50° incidence angle range. In the context of the SMOS and SMAP 4 K brightness temperature error budgets, a rock fraction of ~0.2 may induce a brightness temperature effect in excess of 4 K in horizontal polarization, while a rock fraction of ~0.4 is required in vertical polarization to have the same effect.

To validate the model simulated rock fraction impact on soil moisture retrieval accuracy under bare dry soil conditions (soil moisture of 0.04 m<sup>3</sup>/m<sup>3</sup>), the bulk soil moisture of each 100 m pixel was retrieved from the airborne observations without accounting for the presence of rock using the soil parameters listed in Table 3, and then the observed rock induced soil moisture error was calculated as the difference between retrieved soil moisture and mean ground soil moisture

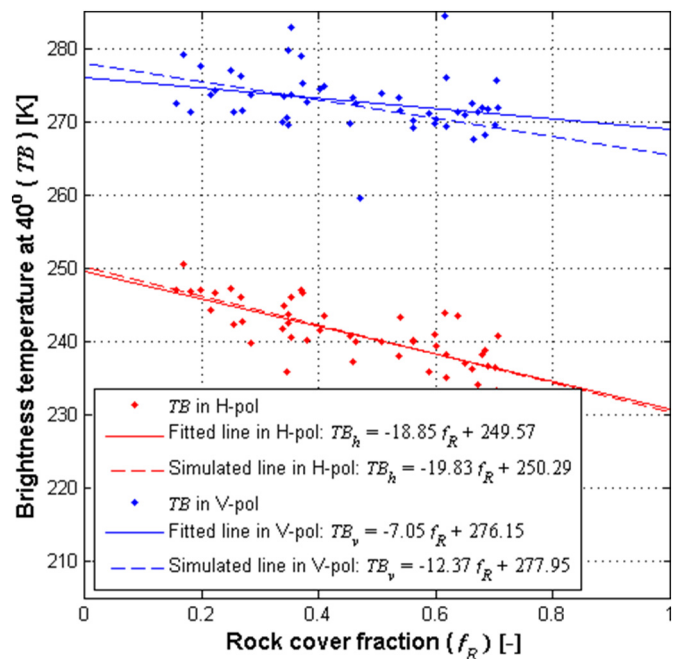


**Fig. 6.** The relationship between rock fraction and the fitted brightness temperature observations at the incidence angle of 40°.

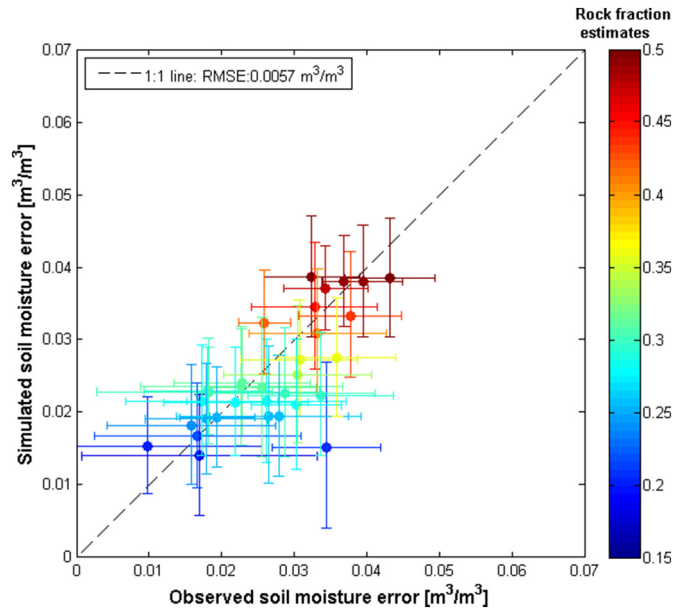


**Fig. 7.** Comparison of the observed and simulated soil moisture errors induced by the presence of rock with a range of cover fractions over the Wirrangula Hill study area. The horizontal whiskers show the standard deviation of soil moisture error between retrieved and ground measured soil moistures for each pixel, while the vertical whiskers show the variation of simulated soil moisture error caused by the rock cover fraction uncertainty of 0.19.

measurements within the given pixel as ground truth. Subsequently, the simulated rock induced soil moisture error was modelled for rock fraction and soil moisture of the given pixel through L-MEB.

Fig. 7 shows the comparison between observed and simulated rock induced soil moisture errors for the range of rock cover fractions over the Wirrangula Hill study area. To account for the uncertainties of ground soil moisture measurements and rock fraction estimates, horizontal whiskers indicate the standard deviation of HDAS soil moisture measurements within each pixel, while vertical whiskers indicate the

variation of simulated soil moisture error derived from the pixel rock cover fraction plus and minus the standard deviation of estimated rock cover fraction of 0.19. A good agreement was found between observed and simulated impacts of rock fraction on soil moisture retrieval accuracy with a RMSE of  $0.0057 \text{ m}^3/\text{m}^3$ . Moreover, it was found that ignoring even a 0.1 rock fraction in the retrieval model can induce error in the retrieved soil moisture of  $\sim 0.01 \text{ m}^3/\text{m}^3$  over dry bare soil. In the context of the SMOS and SMAP soil moisture target accuracy of  $0.04 \text{ m}^3/\text{m}^3$ , it was confirmed that an approximately 0.4 rock cover fraction can be tolerated under dry bare soil conditions before unacceptable errors occur. Consequently, it is proposed that the threshold of 0.4 can be used to identify the SMOS and SMAP pixels globally where rock-induced soil moisture error may potentially exceed the error budget.

## 6. Rock impact estimation at global scale

In the SMOS Level 2 soil moisture retrieval algorithm, Eoclimap (Masson et al., 2003) is used as the reference land cover dataset, due to its high resolution and fine land surface classification (Kerr et al., 2010). The Eoclimap was developed to initialize the soil-vegetation-atmosphere transfer schemes (SVATs) in meteorological and climate models. Two hundred and fifty ecosystems with homogeneous vegetation were derived from a combination of two global land cover datasets (IGBP/DIS and University of Maryland database; Hansen et al., 2000; Loveland and Belward, 1997; Loveland et al., 2000), the map of the terrestrial climates (Koeppen and De Long, 1958), and the Normalized Difference Vegetation Index (NDVI) data of the Advanced Very High Resolution Radiometer (AVHRR) satellite. The global surface parameter at a resolution ranging from 30 s to  $1^\circ$  can be extracted from the Eoclimap by integrating the 30 s data. Consequently, the rock distribution data at the resolution of 30 s were extracted from the Eoclimap 2004, and resampled to the SMOS DGG (Discrete Global Grid) and the SMAP EASE (Equal-Area Scalable Earth) grids. All SMOS and SMAP pixels over the global land mass were categorized based on rock fraction impacts on brightness temperature and soil moisture retrieval accuracy, to six levels: i) rock free pixels with no rock-induced brightness temperature impact or subsequent soil moisture retrieval errors; ii) pixels with rock fraction  $< 0.05$ , interpreted as rock induced brightness temperature contribution less than the SMAP L-band radiometric uncertainty of 1.3 K (Entekhabi et al., 2010) for horizontal polarization, and rock induced soil moisture retrieval error  $< 0.005 \text{ m}^3/\text{m}^3$ ; iii) pixels with rock fraction  $< 0.1$ , interpreted as rock induced brightness temperature contribution less than the SMAP L-band radiometric uncertainty of 1.3 K for vertical polarization, and rock induced soil moisture retrieval error  $< 0.01 \text{ m}^3/\text{m}^3$ ; iv) pixels with rock fraction  $< 0.2$ , interpreted as rock induced brightness temperature contribution  $< 4 \text{ K}$  for horizontal polarization and 2 K for vertical polarization, and rock induced soil moisture retrieval error  $< 0.02 \text{ m}^3/\text{m}^3$ ; v) pixels with rock fraction  $< 0.4$ , interpreted as rock induced brightness temperature contribution  $< 8 \text{ K}$  for horizontal polarization and 4 K for vertical polarization, and rock induced soil moisture retrieval error  $< 0.04 \text{ m}^3/\text{m}^3$ ; and vi) pixels with rock fraction  $> 0.4$ , interpreted as rock induced brightness temperature contribution  $> 8 \text{ K}$  for horizontal polarization and 4 K for vertical polarization, and rock induced soil moisture retrieval error  $> 0.04 \text{ m}^3/\text{m}^3$  (Table 4).

Due to the similar footprint size of SMOS and SMAP, this paper only shows a single plot of rock affected pixels (Fig. 8). The fraction of rock affected pixels of both the SMOS and SMAP missions were calculated for the main continents and listed in Table 5. It can be seen that rock is not homogeneously distributed across the globe. There are  $> 1.5\%$  SMOS and SMAP pixels with a rock cover fraction exceeding the 0.4 threshold globally, potentially inducing a soil moisture retrieval error exceeding the target accuracy of  $0.04 \text{ m}^3/\text{m}^3$  under very dry or wet conditions. In Asia,  $> 3\%$  of SMOS and SMAP pixels may be affected by the presence of rock induced soil moisture retrieval errors in excess of

**Table 4**

Rock induced error in brightness temperature ( $\text{TB}_h$  and  $\text{TB}_v$ ) and soil moisture (SM) for a range of surface rock cover fractions referred to as rock impact level.

	1	2	3	4	5	6
Rock fraction [–]	0	0–0.05	0.05–0.1	0.1–0.2	0.2–0.4	$> 0.4$
Rock induced $\text{TB}_h$ impact [K]	0	0–1	1–2	2–4	4–8	$> 8$
Rock induced $\text{TB}_v$ impact [K]	0	0–0.5	0.5–1	1–2	2–4	$> 4$
Rock induced SM error [ $\text{m}^3/\text{m}^3$ ]	0	0–0.005	0.005–0.01	0.01–0.02	0.02–0.04	$> 0.04$

the soil moisture error budgets. There are 80 SMOS pixels over Asia, Africa and South America having full rock coverage and the largest expected error of  $0.1 \text{ m}^3/\text{m}^3$  in retrieved soil moisture. These rock impact maps can be used to mask affected pixels or flag the rock induced uncertainty in the absence of accounting for rock effects in the soil moisture retrieval of SMOS and SMAP. It should be noticed that many rock impacted pixels are located in mountainous regions (North America, South America, Himalayas, and Alps) where the SMOS and SMAP brightness temperature and soil moisture are also affected by topography, and therefore have no retrieved soil moisture values in any case.

## 7. Conclusions

Both the European Space Agency's (ESA) Soil Moisture and Ocean Salinity (SMOS) and the National Aeronautics and Space Administration's (NASA) Soil Moisture Active Passive (SMAP) satellites employ a L-band (1.41 GHz) radiometer to measure microwave emission from the land surface globally every 2–3 days, which is used to retrieve the top  $\sim 5 \text{ cm}$  soil moisture through a radiometric transfer model. However, this technique suffers from its coarse  $40 \text{ km}$  spatial resolution, due to technical limitations on current state-of-the-art antenna design. Consequently, large proportions of surface rock in the SMOS and SMAP field-of-view will likely confound the interpretation of brightness temperature observations, resulting in soil moisture retrieval errors that exceed the SMOS and SMAP  $0.04 \text{ m}^3/\text{m}^3$  target accuracy if not accounted for in the retrieval process. Thus, this study has focused on understanding the rock effect using both synthetic data and observations collected during an airborne field experiment.

Previous studies on rock effects have suggested that rock can be assumed to behave like a very dry bare soil with a fixed dielectric constant of  $5.7 \cdot j \times 0.074$ . Using this assumption, the microwave emission from the land surface was simulated for various rock cover fraction, soil moisture and vegetation content conditions using the  $\tau\omega$  model. The simulation results showed that the effects of rock fraction on brightness temperature and soil moisture retrieval accuracy are dependent mainly on water content of the surrounding soil. Under dry soil conditions, rock introduces a decrease in bulk brightness temperature and an overestimation of retrieved soil moisture, while causing an increase in bulk brightness temperature and an underestimation of retrieved soil moisture under wet soil conditions, if not accounting for the presence of rock in the soil moisture retrieval model. Moreover, for the SMOS and SMAP target accuracy of  $0.04 \text{ m}^3/\text{m}^3$  and 4 K brightness temperature uncertainty, rock cover fraction thresholds of 0.4 and 0.2 for very dry conditions were obtained respectively. These thresholds have been used to identify SMOS and SMAP pixels that are expected to have rock induced soil moisture error exceeding the error budget.

The rock effects identified from simulation were validated using airborne passive microwave observations and ground soil moisture measurements collected during a field campaign in central Australia. In the Wirrangula Hill study area, L-band (1.413 GHz) brightness temperature at  $\sim 100 \text{ m}$  resolution were used together with top  $\sim 5 \text{ cm}$  soil

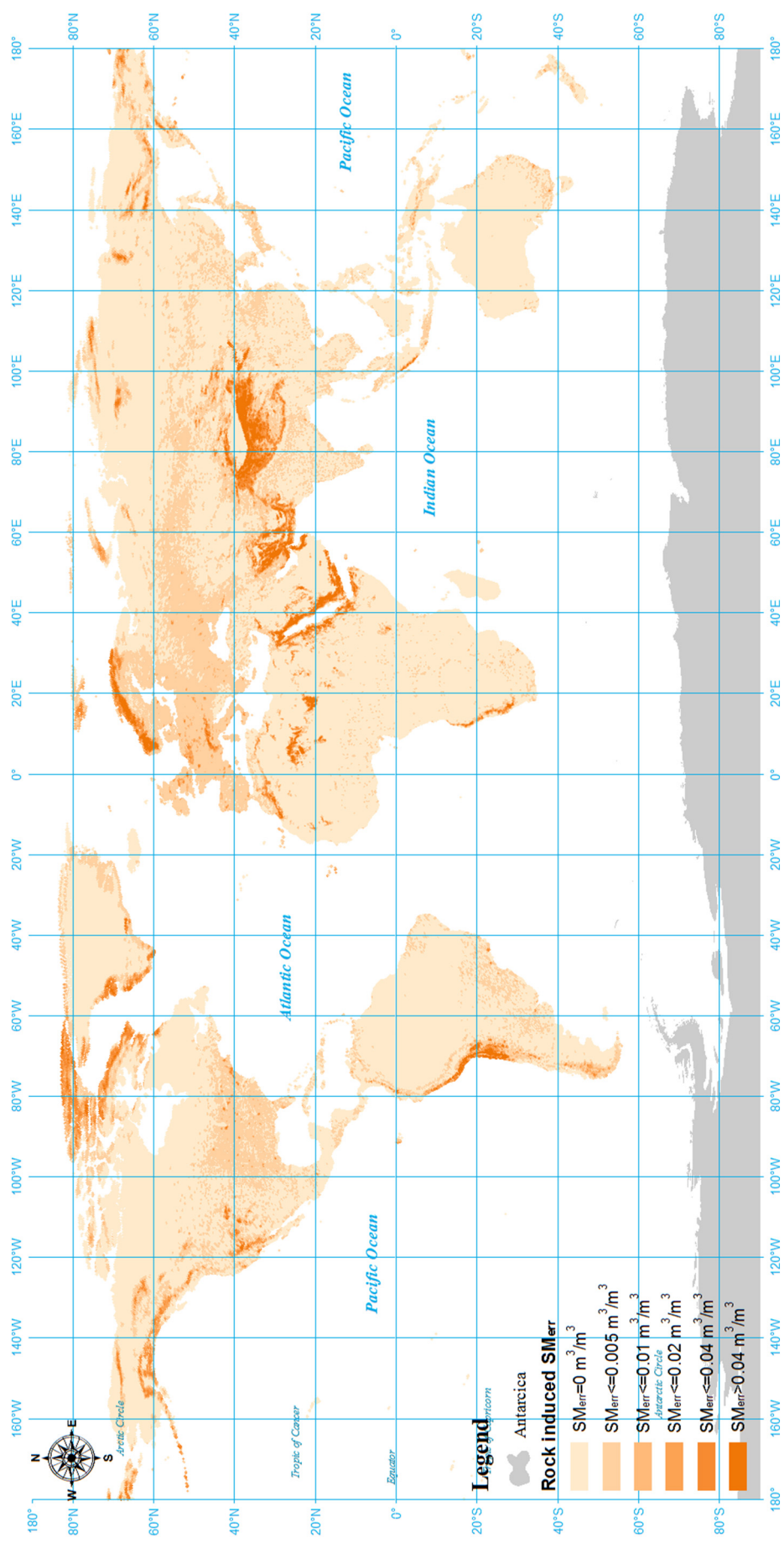


**Fig. 8.** Distribution of rock impacted pixels of SMOS over global land mass, based on levels of rock effects listed in Table 4.

**Table 5**

Statistics of the SMOS and SMAP pixels with rock impact at each level.

Level		1	2	3	4	5	6
Percentage of the SMOS and (SMAP) pixels [%]	Africa	87.2 (87.5)	7.8 (7.6)	1.3 (1.2)	1.4 (1.3)	1.3 (1.3)	1.0 (1.0)
	Asia	65.0 (67.4)	24.0 (22.3)	2.3 (2.2)	2.5 (2.4)	3.1 (2.7)	3.2 (3.0)
	Europe	24.1 (27.3)	67.1 (64.2)	3.7 (3.6)	2.2 (2.3)	1.5 (1.4)	1.4 (1.2)
	North America	66.0 (66.8)	27.6 (26.6)	2.2 (2.3)	2.3 (2.6)	1.7 (1.6)	0.2 (0.1)
	Oceania	94.5 (94.6)	5.2 (5.1)	0.1 (0.2)	0.1 (0.1)	0.0 (0.0)	0.0 (0.0)
	South America	82.0 (82.5)	13.7 (13.1)	1.2 (1.3)	1.1 (1.3)	0.9 (0.8)	1.0 (1.0)
	Global	71.1 (72.0)	21.7 (21.1)	1.9 (1.9)	1.9 (1.9)	1.8 (1.7)	1.6 (1.4)

moisture point measurements within a 700 m × 3000 m focus area, characterized by bare soil covered with very sparse bush, and rock fractions of up to 1.0. Using a Google Earth image and ground level photographs over the study area, a relationship between gray intensity and rock fraction was established for estimating the rock cover fraction within the focus area.

To identify the SMOS and SMAP pixels with expected rock-induced soil moisture error in excess of the 4 K and 0.04 m<sup>3</sup>/m<sup>3</sup> error targets globally, the fraction thresholds identified by this study were applied to the global rock distribution map extracted from the Ecoclimap dataset, which is the land surface map for the SMOS L2 retrieval algorithm. Over land, approximately 3.3% of all SMOS and SMAP pixels were found to have brightness temperature error potentially exceeding 4 K. The most affected continent is expected to be Asia, with up to 6.0% of the SMOS and SMAP pixels exceeding the 4 K brightness temperature error thresholds. When assessing the impact on soil moisture retrieval basis using the 0.04 m<sup>3</sup>/m<sup>3</sup> target accuracy, this reduced to 1.5% of SMOS and SMAP pixels globally and 3.0% of pixels in Asia. While these results might be conservative, as they assume that the entire soil moisture error budget can be attributed to rock induced effects alone, the need to consider rock cover fraction of global soil moisture monitoring is highlighted.

## Acknowledgements

This study has been conducted within the framework of the MoistureMap project funded by the Australian Research Council (DP0879212). Access and accommodation at Wirrangula Hill was provided by Trevor Williams of the Nilpinna cattle station and his hospitality is hereby gratefully acknowledged. The authors would also like to acknowledge the invaluable field work assistance of Mahdi Allahmoradi, Justin Costelloe, Susan Hayes, Jon Johansson, Alan Marks, Vjeko Matic, Sandy Peischl, Peter Richardson, Graeme Tomlinson, and all participants of the field experiment in 2003. Hangar space for the research equipment at the Coober Pedy airport was provided by Opal Air. Contributions by Airborne Research Australia, Flinders University are also acknowledged.

## References

- Cano, A., Saleh, K., Wigneron, J.-P., Antolín, C., Balling, J.E., Kerr, Y.H., Kruszewski, A., Millán-Scheidig, C., Søbjærg, S.S., Skou, N., 2010. The SMOS Mediterranean Ecosystem L-Band characterisation Experiment (MELBEX-I) over natural shrubs. *Remote Sens. Environ.* 114, 844–853.
- Crow, W.T., Berg, A.A., Cosh, M.H., Loew, A., Mohanty, B.P., Panciera, R., de Rosnay, P., Ryu, D., Walker, J.P., 2012. Upscaling sparse ground-based soil moisture observations for the validation of coarse-resolution satellite soil moisture products. *Rev. Geophys.* 50, RG2002.
- Delwart, S., Bouzinac, C., Wursteisen, P., Berger, M., Drinkwater, M., Martín-Neira, M., Kerr, Y.H., 2008. SMOS validation and the COSMOS campaigns. *IEEE Trans. Geosci. Remote Sens.* 46, 695–704.
- Dobson, M.C., Ulaby, F.T., Hallikainen, M.T., El-Rayes, M.A., 1985. Microwave dielectric behavior of wet soil-part II: dielectric mixing models. *Geoscience and Remote Sensing, IEEE Transactions on* 35–46.
- Entekhabi, D., Njoku, E.G., O'Neill, P.E., Kellogg, K.H., Crow, W.T., Edelstein, W.N., Entin, J.K., Goodman, S.D., Jackson, T.J., Johnson, J., 2010. The soil moisture active passive (SMAP) mission. *Proc. IEEE* 98, 704–716.
- Hansen, M.C., DeFries, R.S., Townshend, J.R.G., Sohlberg, R., 2000. Global land cover classification at 1 km spatial resolution using a classification tree approach. *Int. J. Remote Sens.* 21, 1331–1364.
- Jackson, T.J., Kostov, K.G., Saatchi, S.S., 1992. Rock fraction effects on the interpretation of microwave emission from soils. *IEEE Trans. Geosci. Remote Sens.* 30, 610–616.
- Jackson, T.J., Schmugge, T.J., 1989. Passive microwave remote sensing system for soil moisture: some supporting research. *IEEE Trans. Geosci. Remote Sens.* 27, 225–235.
- Jackson, T.J., Schmugge, T.J., 1991. Vegetation effects on the microwave emission of soils. *Remote Sens. Environ.* 36, 203–212.
- Kerr, Y.H., Waldteufel, P., Richaume, P., Davenport, I., Ferrazzoli, P., Wigneron, J.-P., 2010. SMOS Level 2 Processor Soil Moisture Algorithm Theoretical Basis Document (ATBD). SM-ESL (CSBA), CESBIO, Toulouse (SO-TN-ARR-L2PP-0037, Issue 3.4).
- Kerr, Y.H., Waldteufel, P., Richaume, P., Wigneron, J.-P., Ferrazzoli, P., Mahmoodi, A., Al Bitar, A., Cabot, F., Gruhier, C., Juglea, S.E., 2012. The SMOS soil moisture retrieval algorithm. *IEEE Trans. Geosci. Remote Sens.* 50, 1384–1403.
- Kerr, Y.H., Waldteufel, P., Wigneron, J.-P., Delwart, S., Cabot, F., Boutin, J., Escorihuela, M.J., Font, J., Reul, N., Gruhier, C., 2010. The SMOS mission: new tool for monitoring key elements of the global water cycle. *Proc. IEEE* 98, 666–687.
- Koeppen, C.E., De Long, G., 1958. Weather and Climate.
- Loew, A., 2008. Impact of surface heterogeneity on surface soil moisture retrievals from passive microwave data at the regional scale: the Upper Danube case. *Remote Sens. Environ.* 112, 231–248.
- Loveland, T.R., Belward, A.S., 1997. The IGBP-DIS global 1 km land cover data set, DISCover: first results. *Int. J. Remote Sens.* 18, 3289–3295.
- Loveland, T.R., Reed, B.C., Brown, J.F., Ohlen, D.O., Zhu, Z., Yang, L., Merchant, J.W., 2000. Development of a global land cover characteristics database and IGBP DISCover from 1 km AVHRR data. *Int. J. Remote Sens.* 21, 1303–1330.
- Masson, V., Champeaux, J.L., Chauvin, F., Meriguet, C., Lacaze, R., 2003. A global database of land surface parameters at 1-km resolution in meteorological and climate models. *J. Clim.* 16, 1261–1282.
- Merlin, O., Walker, J.P., Panciera, R., Young, R., Kalma, J.D., Kim, E.J., 2007. Calibration of a soil moisture sensor in heterogeneous terrain with the National Airborne Field Experiment (NAFE) Data. In: Oxley, L., Kulasiri, D. (Eds.), MODSIM 2007 International Congress on Modelling and Simulation. Modelling and Simulation Society of Australia and New Zealand, pp. 2604–2610.
- Mironov, V.L., Dobson, M.C., Kaupp, V.H., Komarov, S.A., Kleshchenko, V.N., 2004. Generalized refractive mixing dielectric model for moist soils. *IEEE Trans. Geosci. Remote Sens.* 42, 773–785.
- Mo, T., Choudhury, B.J., Schmugge, T.J., Wang, J.R., Jackson, T.J., 1982. A model for microwave emission from vegetation-covered fields. *J. Geophys. Res.* 87 (11229–11231, 11237).
- Monerris, A., Vall-Llossera, M., Camps, A., Piles, M., 2008. Rock fraction effects on the surface soil moisture estimates from L-band radiometric measurements. In: IGARSS 2008–2008 IEEE International Geoscience and Remote Sensing Symposium. IEEE (pp. II-711-II-714).
- Njoku, E.G., Wilson, W.J., Yueh, S.H., Dinardo, S.J., Li, F.K., Jackson, T.J., Lakshmi, V., Bolten, J., 2002. Observations of soil moisture using a passive and active low-frequency microwave airborne sensor during SGP99. *IEEE Trans. Geosci. Remote Sens.* 40, 2659–2673.
- Owe, M., de Jeu, R., Walker, J.P., 2001. A methodology for surface soil moisture and vegetation optical depth retrieval using the microwave polarization difference index. *IEEE Trans. Geosci. Remote Sens.* 39, 1643–1654.
- Panciera, R., Merlin, O., Young, R., Walker, J.P., 2006. The Hydraprobe Data Acquisition System (HDAS): User Guide (p. 24). University of Melbourne, Melbourne, Australia.
- Panciera, R., Walker, J.P., Kalma, J.D., Kim, E.J., Hacker, J.M., Merlin, O., Berger, M., Skou, N., 2008. The NAFE'05/CoSMOS data set: toward SMOS soil moisture retrieval, downscaling, and assimilation. *IEEE Trans. Geosci. Remote Sens.* 46, 736–745.
- de Rosnay, P., Drusch, M., Boone, A., Balsamo, G., Decharme, B., Harris, P., Kerr, Y., Pellarin, T., Polcher, J., Wigneron, J.-P., 2009. AMMA land surface model inter-comparison experiment coupled to the community microwave emission model: ALMIP-MEM. *J. Geophys. Res.* 114, D05108.
- Rüdiger, C., Walker, J.P., Kerr, Y.H., Kim, E.J., Hacker, J.M., Gurney, R.J., Barrett, D., Le Marshall, J., 2014. Toward vicarious calibration of microwave remote-sensing satellites in arid environments. *IEEE Trans. Geosci. Remote Sens.* 52, 1749–1760.
- Ryu, D., Famiglietti, J.S., 2006. Multi-scale spatial correlation and scaling behavior of surface soil moisture. *Geophys. Res. Lett.* 33, L08404.
- Sellers, P.J., Dickinson, R.E., Randall, D.A., Betts, A.K., Hall, F.G., Berry, J.A., Collatz, G.J., Denning, A.S., Mooney, H.A., Nobre, C.A., 1997. Modeling the exchanges of energy, water, and carbon between continents and the atmosphere. *Science* 275, 502–509.
- Ulaby, F.T., Moore, R.K., Fung, A.K., 1986. Microwave remote sensing: active and passive. In: Volume Scattering and Emission Theory, Advanced Systems and Applications.

- Volume III.
- Van de Griend, A.A., Wigneron, J.-P., 2004. The b-factor as a function of frequency and canopy type at H-polarization. *IEEE Trans. Geosci. Remote Sens.* 42, 786–794.
- Walker, J., Grayson, R., Panciera, R., Zhan, X., Houser, P., 2003. AMSR-E Soil Moisture Validation Efforts In the Australian Arid Zone. *AGU Fall Meeting Abstracts* (p. 05).
- Wang, J.R., Schmugge, T.J., 1980. An empirical model for the complex dielectric permittivity of soils as a function of water content. *IEEE Trans. Geosci. Remote Sens.* 288–295.
- Wigneron, J.-P., Kerr, Y.H., Waldteufel, P., Saleh, K., Escorihuela, M.J., Richaume, P., Ferrazzoli, P., De Rosnay, P., Gurney, R., Calvet, J.C., 2007. L-band microwave emission of the biosphere (L-MEB) model: description and calibration against experimental data sets over crop fields. *Remote Sens. Environ.* 107, 639–655.
- Wigneron, J.-P., Laguerre, L., Kerr, Y.H., 2001. A simple parameterization of the L-band microwave emission from rough agricultural soils. *IEEE Trans. Geosci. Remote Sens.* 39, 1697–1707.